

# GAMMA-RAY TOMOGRAPHY OF IRRADIATED CANDU<sup>®</sup> REACTOR FUEL

BARBARA D. SAWICKA

AECL, Chalk River Laboratories, Chalk River, Ontario K0J 1J0 Canada

## ABSTRACT

Gamma ray computerised tomography (CT) methods have been developed to measure the porosity distribution, cracking pattern, and other characteristics of irradiated CANDU<sup>®</sup> power reactor fuel pellets. This paper illustrates the technique and documents a CT study of two 24-mm-long sections of CANDU reactor UO<sub>2</sub> fuel elements. Transmission CT was used to map porosity at various longitudinal cross-sections, and to evaluate dish filling, fuel swelling, three-dimensional cracking patterns and crack sizes. Emission CT was used to map approximate distributions of accumulated non-volatile fission products and to extract corrections for transmission scans. This work shows that we currently have a unique quantitative method of non-destructively mapping porosity and cracking in irradiated fuel. The CT techniques are non-destructive and non-invasive. The obtained information is complementary to post-irradiation examination of irradiated fuel by microscopy and ceramography.

## INTRODUCTION

CANDU<sup>®</sup> reactor fuel currently comprises natural UO<sub>2</sub> pellets in 28- or 37-element bundles. Each element contains a number of cylindrical pellets of sintered UO<sub>2</sub> in a Zircaloy sheath. During irradiation, dimensional and microstructural changes take place within the fuel pellets; these changes include enhanced plasticity, densification and swelling resulting from high temperature and temperature gradients, as well as the release, migration and accumulation of fission products. Dimensional changes affect fuel performance by influencing cladding strain and heat transfer.

The behaviour of fuel elements and assemblies during irradiation varies considerably depending on reactor operating parameters and on subtle differences in fuel design. Key operating parameters include fuel burnup, linear power and peak sheath temperature. Fuel design parameters include fuel composition, density, microstructure and dimensions; axial and radial clearance; and the thickness, composition and microstructure of the cladding material.

Understanding fuel properties is critical to ensure efficient and safe operation of CANDU reactors. Since the 1950s, much work has gone into understanding, measuring and modelling fission-gas release during irradiation of nuclear fuels. This continues to be an important subject as current fuels are taken to higher burnups, and mixed oxide (MOX) and thoria fuels are developed. Post-irradiation examination (PIE) of irradiated fuel is performed at AECL to provide data on fuel characteristics. These data are used to correct and validate fuel-performance modelling codes, and to facilitate performance enhancements to existing and future fuel-element and fuel-bundle designs. Many techniques have been employed over the last five decades in post-irradiation examination (PIE), including visual examination, profilometry, gas

---

<sup>®</sup> CANDU is a registered trademark of Atomic Energy of Canada Limited (AECL).

puncture and analysis, isotopic analysis, gamma-beta-alpha radiography, ceramography and metallography, and scanning electron microscopy (SEM). The obtained data and the knowledge gained provide input for theoretical modelling and fuel performance codes. This continues to be an important subject as MOX and thoria fuels are developed, and as higher burnups of slightly enriched  $\text{UO}_2$  are to be used in the future Advanced CANDU Reactor™ design.

The goal of the current work was to explore the possibility of using CT techniques in PIE of irradiated fuel. One important issue was to explore whether CT can be used to measure porosity distribution and radial porosity gradient, which is used to characterize the extent of gas bubble formation due to fission-product release during irradiation. Radial porosity gradients have been evaluated using liquid immersion of fuel microsamples – a technique that was found to be inaccurate, as well as dose- and labour-intensive.

Computerised tomography (CT) methods have been used in the past at AECL in a range of applications to characterise structures, materials and processes. There are two types of applications that are relevant to the current work: the measurement of defects and the mapping of density gradients in green and sintered ceramics; and the evaluation of structural damage details in severe fuel-damage tests [1–7].

This report documents the development of CT-based experimental techniques to evaluate porosity gradients in, and dimensional characteristics of, irradiated  $\text{UO}_2$  fuel. First experiments were reported earlier [8]. Key features of the techniques are illustrated here with results from two sections of irradiated CANDU reactor fuel elements.

## EXPERIMENTAL PROCEDURES

### CT Imaging and Density Mapping

Computerised tomography is an imaging technique that produces cross-sectional maps of an object. The images are calculated from non-invasive measurements that are performed outside of the test object [9].

A CT scan is performed by measuring projection data, i.e., a series of line integrals at various angles and positions in a cross-sectional plane of the test object. In transmission tomography (t-CT), line integrals are count rates of gamma- or X-radiation from an external radiation source:

$$I_i = \int I_o(E) \exp[-\int LAC(x,y,E) ds] dE$$

where  $I_i$  is the number of photons transmitted through the object,  $I_o$  is the number of incident photons,  $LAC$  is the linear attenuation coefficient (for the radiation energy  $E$  and the material at location  $(x,y)$  in the examined object), and  $s$  is the length along the radiation beam per ray through the examined object. A set of line integrals measured at one angle is called a projection. Transmission-CT projections measured for irradiated fuel contain a component of the gamma radiation signal from radioactive fission products, which needs to be taken into account before the image is calculated. Without energy integration the formula is valid for a monoenergetic radiation beam.

Emission tomography is measured without an external radiation source; it can be performed on objects that contain radioactive species, such as fission products in irradiated fuel. Line integrals then reflect the distribution of radioisotopes,  $\varphi(x,y)$ , in the measured cross-section and path:

$$I_i = \iint \varphi(x,y,E) \exp[-\int LAC(x,y,E) ds] ds' dE .$$

---

™ Advanced CANDU Reactor is a trademark of AECL.

A two-dimensional (2-D) image is calculated from the measured projection data as a matrix of pixels that represent the *LAC* distribution,  $LAC(x,y) = LAC_{ij}$ , or density,  $\rho(x,y) = \rho_{ij}$ , in transmission CT and the distribution of radioactive species,  $\mu(x,y) = \mu_{ij}$ , in emission CT. Emission CT could map the distribution of selected individual isotopes, using the detector focussed to an energy that is specific to a selected radioactive isotope. Several 2-D images are combined into a 3-D image to reconstruct the volume.

CT images measured in the transmission mode illustrate internal structures and the density distribution. Density changes can show porosity gradients, pores and various other geometrical shapes, e.g., cracks, and low- and high-density inclusions. Material porosity has no influence on the precision of the density data, unless it is accompanied by a change in material composition. If the CT image resolves volume elements that are sufficiently small to be treated as homogeneous, then the reconstructed image will not be limited by the material composition. CT images can also provide accurate quantitative data on geometrical dimensions, density gradients and densities.

The CT image  $LAC_{ij}$  can be recalculated to represent a pixel map of absolute density,  $\rho$ , in  $\text{g/cm}^3$ , using mass attenuation coefficients, *MACs*, which for known materials and radiation energies used for scanning can be calculated from theoretical *MACs* for individual elements known for a wide energy range [10, 11]. For monoenergetic radiation,  $\rho(x,y) = \rho_{ij} = LAC_{ij}/MAC$ . For radiation sources with multi-energy lines, such as  $^{192}\text{Ir}$  used in this work and X-ray generators, beam-hardening (*BH*) corrections are required to account for effects that result from the radiation beam energy distribution. The *BH* correction method used in this work consists in calculating corrections to individual data points,  $I_i$ , using an iterative process and using known data on radiation source yields and energies, and detector efficiencies and *MAC* values for individual energy lines. Exact *BH* corrections are possible for radio-isotopic radiation sources, because of their well-defined and stable energy spectra. X-ray generators, which are typically used in standard CT and are preferred when high throughput is required, provide less accurate results because of their unstable, broad-energy spectra. The use of isotopic sources and the high-accuracy, first-generation scanner were essential in this work to measure densities in absolute units (in  $\text{g/cm}^3$ ), to permit density gradient measurements with high precision, and to evaluate microporosity.

A pixel in a 2-D CT image is associated with the volume of a voxel whose height equals the "in-slice" thickness of the measured cross-section determined by the radiation beam width in the scanning plane. The spatial resolution within the measured cross-section is determined by the radiation beam geometry and the spacing between individual ray paths used in the scanning process. A CT value for an individual pixel (voxel) bears an error that limits the CT data precision. This error is defined by the image noise or contrast and can be measured as the pixel-to-pixel fluctuations within a *LAC*-uniform region in the calculated image. The main contribution to this error comes from the radiation counting statistics—longer counting times result in better statistics and lower error. By averaging the CT data over several or many pixels, an increased precision in density measurement can be achieved in comparison to the pixel density.

A CT image is displayed using grey levels or colours corresponding to selected ranges of CT values or densities. Because a human eye can view only a limited range of colours or grey shades, different scale ranges must be used to view all the details. Each displayed or printed image shows only one, subjectively selected representation of the data, and it usually does not show all the features that are recorded. Printed images provide some illustration of the observed features, however, quantitative data, such as density gradients, densities in  $\text{g/cm}^3$  and crack sizes are evaluated from numerical CT data.

Projection and image data are archived and are available for re-evaluation and mathematical processing. Data processing methods used in this work included algebraic operations, noise reduction, data filtering, statistical calculations, morphology functions, etc. [12, 13].

## Irradiated Fuel and CT Scan Geometry

Experiments were performed on two small sections of irradiated fuel, from two standard CANDU fuel bundles. Both fuel sections were 24 mm long, in a Zircaloy sheath, and were cut from the middle part of an outer-ring fuel element. Each contained one whole pellet, 12.2 mm in diameter and 16 mm in length, and about half of the adjacent pellet, hence comprising an interface region (dish area) between two pellets. Figure 1 shows the location of the cut sections in the two fuel elements and the location of CT scans in both sections. CT scans were performed perpendicular to the axis of the fuel pellet to measure radial cross-sections. Scan locations are marked in Figure 1 as a distance  $x$  from the pellet top (dish) relative to the pellet length  $L$ .

The two fuels taken for CT examination differed slightly in some pre-irradiation characteristics, including density, grain size, axial gap and diametrical clearance. Their irradiation characteristics were very different. Fuel element Y was prepared with some modification of the standard procedure to achieve a controlled variance in density and clearance: its pre-irradiation density was  $10.48 \text{ g/cm}^3$ . It was irradiated at a linear power of about  $45 \text{ kW/m}$  to a burnup of  $161 \text{ MWh/kgU}$ , which is typical for CANDU reactors. Fuel element J was manufactured according to standard specifications for CANDU and its pre-irradiation density was  $10.70 \text{ g/cm}^3$ . The irradiation was performed to a burnup of  $540 \text{ MWh/kgU}$  (which is about three times higher than normal), at a power of  $50\text{-}57 \text{ kW/m}$  during the first 25% of the fuel burnup cycle, and at a relatively low power of about  $30\text{-}40 \text{ kW/m}$  during the remaining 75% of the cycle.

## CT Scanner and Special Techniques for Irradiated Fuel

For a CT examination, a section of the irradiated fuel was loaded into the shielding flask and transported to the CT laboratory. The flask design made it suitable for fuel transport and scanning. The flask consists of two hemispheres of 10-cm-thick lead, connected by a 5-mm-high Lucite window, permitting 360-degree access of the external radiation beam to the selected fuel axial location [7]. A CRL-constructed CT scanner was used. It features a so-called *first-generation geometry* with a rotate-translate type of movement, a pencil-shaped radiation beam and parallel ray beams in the projection data [14]. This scanner is capable of providing more accurate images than scanners of other geometries. It also permits the user to select the spatial resolution, contrast and the scanning area by means of a flexible choice of hardware and software parameters. The radiation beam is defined by two tungsten collimators, which provide an aperture that has a height of 1 mm and is flexibly adjustable from 0.01 mm to 2.5 mm in the scanning plane.

Transmission-mode scanning was performed using  $^{192}\text{Ir}$  (20-40 Ci) or  $^{60}\text{Co}$  (10 Ci) radioactive sources that both provide sufficient radiation energy to penetrate the  $\text{UO}_2$  pellet. The  $^{192}\text{Ir}$  source has about 20 energy lines from 100 keV to 900 keV, with an average energy of about 400 keV. The  $^{60}\text{Co}$  is practically mono-energetic, for the  $\text{UO}_2$  pellet material and thickness, with an average energy of 1.25 MeV. The  $^{192}\text{Ir}$  source was used for most measurements because of its much higher yield (beam intensity per unit radioactivity) and therefore higher possible contrast in comparison to  $^{60}\text{Co}$  images measured during the same time. The  $^{60}\text{Co}$  scans were performed to verify the accuracy of the density measurements and to define fine corrections required for the *BH* correction procedure used for  $^{192}\text{Ir}$  scans. Each transmission scan was followed by an emission scan performed at the same geometry. The corresponding transmission and emission line integrals were subtracted, to account for the signal from radioactive species, before t-CT images were calculated. The measured emission projection data were also used to calculate approximate distributions of radioactive species.

Standard CT, which is performed on the entire cross-sectional area of the object, i.e., including the shielding flask, would require prohibitively long scans and large data matrices to reconstruct the pellet area with sufficient spatial resolution. Instead, the so-called *Region-of-Interest (ROI)* CT technique was used, in which a small part (the *ROI*) of an object is scanned using high resolution, and the correct *ROI*

image is calculated after incorporating missing data from the low-resolution scan of the entire cross-section [15]. The *ROI* scans were performed using a spacing distance of 80  $\mu\text{m}$  and a scanning diameter of 20.5 mm. The pellet cross-section was reconstructed using  $10^4$  80- $\mu\text{m}$ -pixels. Standard CT scans were performed using a spacing distance and pixel size of 2.56 mm and a scanning diameter of 328 mm; the pellet cross-section was reconstructed using fewer than 20 pixels. Standard scans were performed to define the pellet position, to outline the *ROI* area, and to provide corrections needed for the *ROI* image calculation. In both procedures, the scanning was performed using 360 projections spaced by 0.5 deg and 256 rays per projection; the sampling distance was equal to the collimator aperture, so that the pixel size in the image matrix was consistent with the spatial resolution and the spatial resolution was equal to two pixels. The spatial resolution element in the *ROI* image is a square with a size of 160  $\mu\text{m}$  x 160  $\mu\text{m}$  and is associated with the volume corresponding to a 1-mm slice thickness along the pellet length. Some *ROI* scans were also made using a spacing distance of 160  $\mu\text{m}$ : the spatial resolution element was 320  $\mu\text{m}$  x 320  $\mu\text{m}$  x 1 mm, the pellet cross-section was reconstructed using  $10^3$  pixels, and the image contrast was improved by a factor of about 6 in comparison to *ROI* scans measured over the same scanning time with twice the resolution. The absorption-free intensity of the radiation beam, needed additionally in the *ROI* procedure, was calculated from measurements performed over several days before and after each scan and incorporated fine corrections to the radiation source decay rate.

The image contrast measured at the pixel level ranged from 3 to 15% in various images. To better illustrate the observed density gradients, Gaussian and 4- or 16-pixel algebraic averaging was used on the image data to create CT images with an improved contrast. Data averaging was also performed over rings at selected radii to calculate radial density gradients with an accuracy of better than 1%. This method practically eliminates contributions to the density error from the image statistics and local porosity fluctuations, and corresponds to measuring porosity using a large number of microsamples.

Figure 2 shows six CT images that reconstruct the mid-section of one of the examined pellets to illustrate the *ROI* method and some of the image processing used. Density variations are observed as a change in gray shade or colour, with darker areas indicating lower density than brighter areas. All *ROI* images reproduce a low-density central region and a pattern of radial cracking. The crack width is exaggerated due to insufficient spatial resolution. Figure 3 illustrates the evaluation of radial density gradients using three methods. A radial gradient can be observed by tracing the density change from pixel to pixel along the pellet diameter; one such profile is illustrated by a dotted line in the top graph and shows a large data scatter due to CT image noise and fluctuations in fuel porosity. Averaging the density data over several or more pixels permits us to obtain density gradients with much better accuracy than the image noise. Data averaging over many pixels at a specific radius corresponds to sampling of a large number of microsamples and results in a significant improvement in the radial gradient measurement.

An unirradiated, standard CANDU-type sintered  $\text{UO}_2$  pellet was examined to obtain a reference for the pre-irradiated density and porosity. This pellet was not from the same fabrication batch as the irradiated pellets, but was fabricated using the standard method of fuel fabrication for CANDU reactors. The CT density of the standard pellet measured from a  $^{60}\text{Co}$  scan and averaged over the pellet cross-section was  $10.66 \pm 0.02 \text{ g/cm}^3$ . This agrees with the bulk density measurement performed using the liquid immersion method and indicates 97% densification of the pre-irradiated sintered fuel pellet. The average density was found to be approximately uniform across the pellet cross-section. A slightly higher density value (less than 1% higher) towards the pellet periphery might be a CT-related artefact or might indicate a remnant density gradient. To obtain the net effect caused by irradiation, the radial gradients for irradiated pellets were calculated by normalising the CT data to the density of the standard pellet measured with the same radiation source. The measurement of the standard unirradiated pellet was repeated before each series of experiments to calculate fine corrections needed to the absolute density measurement depending on the  $^{192}\text{Ir}$  source batch. Corrections of up to 2% were needed to the absolute density, while the radial gradient measurements were practically unaffected by the source batch.

## Corrections for the Presence of Fission Products and Plutonium

Irradiated fuel contains various fission products and actinides that are distributed within the fuel material. Their presence influences the calculation of the irradiated fuel density from the measured CT data. Depending on their abundance, distribution, and chemical composition, the presence of fission products and plutonium may cause the largest errors in the absolute density measurement of the irradiated fuel.

Chemical specification of fission products includes the following four types: gases and other volatile fission products such as halogen elements; metallic particles (Mo, Tc, Ru, Rh, Pd, Ag, Cd, In, Sn, Sb and Te); fission products forming oxide precipitates (Rb, Cs, Ba, Zr, Nb, Mo and Te); and fission products dissolved as oxides in the fuel matrix (Sr, Zr, Nb and rare earth elements) [16]. The formation of specific phases depends on the temperature-dependent solubility of various fission products, and on their mobility, grain growth and transient conditions in the fuel. Among fission products in CANDU fuel, Zr, Mo, Xe, Cs and Nd have significantly higher abundance than other elements; out of a range of actinides only plutonium is present in any significant quantity [17]. The chemical composition of the irradiated fuel could be included in the calculation of the CT density, if the elemental composition and distribution of fission products and Pu were known for specific cross-sections. These data could be obtained from emission scans measured with energy discrimination, which was not performed, or from chemical analysis, which is destructive, labour-intensive and therefore impractical. Instead, the effect of the chemical composition was evaluated based on the database of CANDU fuel properties calculated using computer codes as a function of fuel burnup and reactor power [17]. The interpolation to 180 MWh/kgU gives the following values for fuel Y: 0.77 wt.% of fission products, and 0.39 wt.% Pu. Extrapolation to 540 MWh/kg U gives the following values for fuel J: 2.3 wt.% of fission products, and 0.85 wt.% Pu.

Figure 4 illustrates the range of corrections required for CT density data. The presence of fission products was approximated by four elements with the highest concentrations in irradiated fuel, i.e., Zr, Mo, Xe and Nd. As shown, for fission product concentrations below 1 wt.%, the maximum offset is below  $-0.05 \text{ g/cm}^3$ ; for concentrations of 2 wt.% it is about  $-0.1 \text{ g/cm}^3$ ; and for concentrations of 2.3 wt.% it is about  $-0.12 \text{ g/cm}^3$ . Because the density offsets are about the same for various fission products, the magnitude of the fission product fraction is important rather than its chemical composition. For 1 wt.% Pu the offset is below  $+0.02 \text{ g/cm}^3$ . Vertical lines mark the offsets calculated for Y and J fuels. On average, the density calculated from CT is too low by  $0.03 \text{ g/cm}^3$  for fuel Y and by  $0.11 \text{ g/cm}^3$  for fuel J.

The actual offsets at various locations within the fuel pellet, radially and axially, depend on the fuel material composition in those locations, which follows the distribution of fission products and plutonium in irradiated fuel. This distribution results from complex processes occurring during and after irradiation. Their characteristics for specific fuel and burnup conditions can be calculated using computer codes. The rate of production of fission products and Pu follows the shape of the thermal flux curves (except for the 27% of Pu that is produced from resonance capture in  $^{238}\text{U}$ , which is created very close to the pellet surface), and the resulting distribution depends on the complex dynamics of this process, fuel burnup, the location of fuel elements in the reactor, and the migration and diffusion of various elements during irradiation that can differ largely for various fission products. Generally, more fission products tend to reside at large radii than in the centre. Such distributions were indicated by emission CT scans measured in this work for the fuel J, and by gamma emission auto-radiography for another element of the same fuel bundle. The distribution of plutonium is influenced by the dynamics of thermal neutrons and resonance capture, with the tendency of more plutonium to reside at the periphery than in the centre. Both radial and azimuthal variations of fission-product and Pu concentrations in CANDU fuel are typically below 20% (still lower for centrally located fuel elements) [18, 19]. In this work, the maximum variations were assumed to be as high as 50% and the effect of these variations on the CT density was added to the density error.

## EXPERIMENTAL RESULTS

### Fuel Element Y

Figure 5 shows CT images of 13 cross-sections measured for fuel Y pellets. Ten scans were measured at  $x/L$  between 0.12 and 0.82 in the first pellet; one scan close to the pellet interface at  $x/L \sim 1$ ; and two scans at  $x/L \sim 0.32$  and 0.38 in the second pellet. Figure 5 left shows images that were measured using the spatial resolution of 160  $\mu\text{m}$  (pixel size 80  $\mu\text{m}$ ) and the contrast about 5% (different in various images). Figure 5 right shows the same data after Gaussian-filter averaging: the image contrast is improved to better than 2%. The density range is thresholded to show the details of the fuel material, with brighter shades indicating higher density, similar to Figure 2. By combining 2-D cross-sectional images, a 3-D picture of the pellet interior can be composed that maps density changes and crack patterns along the pellet length.

Radial cracks and fragments of circumferential cracking are observed in most cross-sections. The pattern of cracks shows typical post-irradiation fuel cracking [16]. The crack width is generally exaggerated due to insufficient spatial resolution. The calculations of the real crack width from the density values are discussed later in this paper. Crack pattern in adjacent cross-sections can indicate which cracks extend axially over some distance in the pellet height. No cracks were observed in the interface region, where they can be masked by higher density fluctuations due to the pore size distribution. Dark patches in the CT image at  $x/L = 0.38$  indicate that parts of the fuel material are missing, apparently split off during fuel handling.

The CT image measured at the interface region ( $x/L \sim 1$ ) shows expansion of the fuel material into the gap (dishes) between the two pellets. The dish is filled up in its central region, i.e., at a pellet radius up to about 2.5 mm ( $r/R < 0.4$ ). The filling material is highly porous, which can be inferred from the increased pixel-to-pixel fluctuations in comparison to the pellet material in other regions. It is not clear whether the pellets are fused together or not. High nonuniformity of the filling material and different crack patterns in fuel sections above and below the interface region suggest a lack of fusion between the two pellets. There are two small regions (seen as bright areas in the centre) that have a density above 10  $\text{g/cm}^3$ , which might be the only regions in which the fusion occurred. These two regions cover about 3% of the cross-section, i.e., 15% of the pellet radius.

In most cross-sections, density fluctuations outside of cracks are small, and the density is lower at  $r/R < 0.3$  than at large radii, indicating an increased porosity to 0.5 – 1.5 % in the central regions in comparison to the pellet periphery. In contrast to most cross-sections, at  $x/L = 0.47, 0.52$  and 0.57, i.e., close to the pellet mid-section, density is still lower in the centre and, in addition, there are low-density regions asymmetrically located at larger radii (Figure 5). Large density fluctuations are unexpected for such a low burnup, and there is no known mechanism to cause large density changes in the lower temperature region towards the pellet periphery observed at  $x/L = 0.57$ . The increased porosity and the increased concentration of fission products in the pellet centre would both be well outside of the expected values to account for the observed low density. These asymmetrical regions probably indicate fuel fabrication artefacts in this non-standard fuel pellet, or perhaps fuel handling artefacts, or both. The observed effects cannot be explained by artefacts related to CT scanning as all cross-sections in both irradiated and unirradiated fuel were measured using exactly the same geometry and procedure.

Figure 6 left shows density as a function of pellet radius calculated by CT data averaging over eight 0.8-mm-wide concentric rings at selected radii and a central 1.4-mm-radius circle. Horizontal bars mark the ranges of radial averaging. The data averaging areas included from 3400 pixels in large rings to 230 pixels in the central circle, and excluded crack regions. Data for three cross-sections measured close to the pellet mid-section are not included because of their strongly asymmetric radial density distributions.

Data for an unirradiated  $\text{UO}_2$  pellet are shown for comparison. Vertical bars mark the error of the density measurement, including the effect of the presence of fission products and actinides. As shown in Figure 4, the presence of fission products in fuel Y causes the density shift of  $-0.034 \text{ g/cm}^3$ . The presence of plutonium causes the shift of  $+0.014 \text{ g/cm}^3$ . The effect of 50% variations in the abundance of fission products and plutonium causes the density error of  $\pm 0.02 \text{ g/cm}^3$ , which was added to the CT statistical error of  $\pm 0.05 \text{ g/cm}^3$ . This results in the correction of  $+0.03 \text{ g/cm}^3$  required to the CT density values and the total density error of  $\pm 0.07 \text{ g/cm}^3$ . Alternatively, one can include the density shift and fluctuations in the total asymmetrical error of  $+0.11 \text{ g/cm}^3$  and  $-0.07 \text{ g/cm}^3$ .

Density data for the pellet dish area ( $x/L \sim 1$ ) outline the shape of the dish. A relatively high density indicates that the scan position was not in the centre of the gap. These data reflect a combined effect of a changing gap width between two fuel pellets and a changing density of the fuel material within the thickness of the scanned cross-section.

Figure 6 right shows the CT density data normalized to the measurements on the standard unirradiated fuel pellet and to the pre-irradiated density of fuel Y, to extract the irradiation-induced porosity. The left scale indicates the data normalised to the theoretical density at full densification ( $10.96 \text{ g/cm}^3$ ) and shows the total porosity. Data for the pellet dish area are not included because they predominantly reflect changes in the gap width, with only a small contribution from variation in fuel porosity.

### Fuel Element J

Figure 7 shows CT images for five cross-sections measured for the fuel J pellets. Three scans were measured in the first fuel pellet, at  $x/L = 0.24, 0.53$  and  $0.20$ ; one scan at the interface between the two pellets,  $x/L = 1$ ; and one scan in the second pellet at  $x/L = 0.21$  (Figure 1). The left-hand column shows images measured using a spatial resolution of  $160 \mu\text{m}$  and the contrast from 7% to 10% in various images. The contrast improvement after four-pixel averaging (middle column) resulted in a better visual representation of crack regions and a somewhat better representation of density gradients in the mid-section and the interface, but was still insufficient to observe radial density gradients at three  $x/L \sim 0.2$  cross-sections. The right-hand column shows CT images measured using a spatial resolution of  $320 \mu\text{m}$  and a contrast from 1% to 3% in various images. The use of a bigger collimator aperture for lower resolution scanning resulted in an improved image contrast at the same scanning times as for higher resolution scanning, and permitted the observation of radial density gradients at the pixel level in all cross-sections; however, the crack definition was poorer in these images and therefore they were not used for quantitative evaluation of density gradients.

In all measured cross-sections the density is lower, i.e., the porosity is higher, in the centre of the fuel pellet than at the pellet periphery. The radial density gradient in the pellet mid-section is much stronger than at the pellet ends, but it has the same characteristics: a clearly defined, low-density region close to the pellet centre is observed. The density in the central region indicates an irradiation-induced porosity of 3-4% at  $x/L \sim 0.2$  and  $\sim 12\%$  in the mid-section. The central low-density region in the mid-section is slightly skewed off-centre, apparently the result of the peripheral location of the fuel element in the bundle (the element's portions nearer to the centre of the bundle experience lower fluxes and lower temperatures during irradiation). This effect is not observed in three cross-sections at  $x/L \sim 0.2$  probably because of much smaller density gradients at the pellet ends.

In all cross-sections except the interface region radial cracking is observed. Cracks are narrower at the periphery than in the centre, and small cracks might be too narrow or too short to be detected. Similar to fuel element Y, cracks observed in fuel J were too narrow to be represented correctly by the pixel values. The real crack width is calculated from the density values in the next section. From the pattern of cracks

in different cross-sections one can infer that many cracks or crack segments extend axially over the pellet length. There is no evidence of circumferential cracking.

Figure 8 left shows density as a function of pellet radius calculated by CT data averaging over seven 0.8-mm-wide concentric rings and a central 0.8-mm-radius circle. Crack areas were excluded from density averaging. The asymmetry observed at  $x/L \sim 0.5$  was neglected. For  $x/L \sim 1$ , several 0.32-mm-wide rings were additionally added, to better outline the shape of the pellet dish region. Data for the standard unirradiated  $\text{UO}_2$  pellet, calculated using the same pattern of rings, are included for comparison. Horizontal bars mark the ranges of radial averaging. Vertical bars mark the error of the density measurement, including the effect of the presence of fission products and actinides, which was calculated as follows. As shown in Figure 4, the presence of fission products in fuel J causes a density shift of  $-0.12 \text{ g/cm}^3$ . The presence of plutonium causes a shift of  $+0.014 \text{ g/cm}^3$ . The effect of 50% variations in the abundance of fission products and plutonium causes a density error of  $\pm 0.06 \text{ g/cm}^3$ , which was added to the CT measurement error of  $\pm 0.05 \text{ g/cm}^3$ . This gives a correction to the density value of  $+0.11 \text{ g/cm}^3$  and a total error of  $\pm 0.11 \text{ g/cm}^3$ .

Density profiles for the interface region show expansion of fuel material into the gap between the two pellets; the effect is much more pronounced in fuel J than in fuel Y. Clearly outlined are the pellet chamfer and dish at the fractional radius  $r/R$  from 1 to 0.5; at  $r/R < \sim 0.4$  the dish disappears, instead, there is a region of fairly uniform and relatively high density, about  $8.6 \text{ g/cm}^3$ . The pixel-to-pixel variations in this region, higher than the image noise, indicate a porous material. Similarity of crack patterns above and below the interface region suggests that at least some cracks maintain continuity axially across the dish region and indicates strong material bonding between the two pellets.

Figure 8 right shows the CT density data normalized to the measurements on the standard unirradiated fuel pellet and to the pre-irradiated density of fuel J, to extract the irradiation-induced porosity at various radial locations. The left scale indicates the data normalised to the theoretical density at full densification ( $10.96 \text{ g/cm}^3$ ). Data for the pellet dish area are not included because they predominantly reflect changes in the gap width, with only some contribution from variations in fuel porosity.

### **Crack Detectability and Crack Width Calculation from the Density Change**

Crack detectability and reproduction in a CT image depends on whether the crack signal is above the image noise, rather than on the crack width relative to the pixel size. It depends on the crack geometry (specifically, the crack's width relative to the spatial resolution and the crack's depth, i.e., its extent in the scanning plane thickness), material properties, and CT scan parameters.

Cracks that are wider than the resolution element have their width represented correctly by the pixel number. With the currently used resolutions of  $160 \mu\text{m}$  and  $320 \mu\text{m}$ , only cracks wider than  $160 \mu\text{m}$  and  $320 \mu\text{m}$ , respectively, are represented correctly at the pixel level. Cracks that are narrower are observed as being about 2 pixels wide, independent of their real width, while the CT density along the crack length varies between the fuel density and zero, depending on the real crack width. The real crack width can be calculated from the density change within and outside of the crack regions. The accuracy of these calculations depends on the crack geometry, material characteristics, CT image contrast and other CT characteristics. This method was shown to provide correct sizing for cracks more than 20 times narrower than the pixel size [6, 20], but some assumptions must be made regarding crack geometry. Aside from fine cracks that are not detected, the crack pattern is represented correctly, although within pixel size limitations.

Most cracks observed in CT images in fuels J and Y were narrower than the spatial resolution.

Calculations of the real crack width were performed for typical cracks observed in various cross-sections, assuming a single crack within an individual resolution element and assuming the following two extreme configurations: (1) crack extends axially over 1 mm and (2) crack width is equal in two directions (i.e., axial and radial for circumferential cracks, and axial and circumferential for radial cracks). The crack width was averaged over 0.5- to 4-mm-long crack segments.

The width of typical cracks, calculated as an average for 2-mm long crack segments, ranges from 5  $\mu\text{m}$  for the narrowest cracks to 50  $\mu\text{m}$  for the widest cracks, assuming configuration 1, and from 80 to 160  $\mu\text{m}$  respectively, assuming configuration 2. The accuracy of this evaluation is 5% for the widest cracks and 50% for the narrowest cracks observed. For most cracks, configuration 2 was unrealistic because the calculated width was large enough to be reproduced as being wider than the observed two pixels, and these results were discarded. For the narrowest cracks, mostly at the pellet periphery, either configuration might be correct, and the crack pattern observed in adjacent cross-sections could help to decide which cracks extend axially (configuration 1) and which represent configuration 2. Using 4 mm long crack segments, cracks about 4  $\mu\text{m}$  wide were also measured, mostly at the pellet periphery. No cracks were observed in the interface region where they might be masked by high porosity of the fuel material.

Data in Table 1 illustrate the width of the smallest cracks that are detectable in CT images for  $\text{UO}_2$  fuel pellets using a pixel size of 80  $\mu\text{m}$ . Calculations were performed for two crack configurations as a function of the image contrast, for three lengths of crack segments (5, 10 and 80 pixels, i.e., 0.4 mm, 0.8 mm and 6 mm, respectively), and assuming a single crack within an individual resolution element. The range of values in each cell in Table 1 results from a range of possible crack orientations within a voxel and the assumption of the crack signal to be two to three times above the image noise. For a 160- $\mu\text{m}$  pixel size and the crack length in pixels remaining unchanged (which means that the cracks are twice as long in mm), the numbers are a factor of 2 larger. Bold numbers mark the values for the current scan parameters and crack segments below 1 mm in length. As seen, the smallest cracks that are detectable using the current scan parameters are 5 to 50  $\mu\text{m}$  in size, depending on the length and geometry of the observed cracks. Detection of tighter cracks would require CT imaging with better spatial resolution than that currently used; better contrast would help to some extent, although narrower cracks might still be masked by the statistical noise of the CT image and by density fluctuations due to pore size distribution. Because the limit for crack detection depends on the length of the crack segments, and because crack segments are shorter in circumferential cracks than in radial cracks, circumferential cracks might be somewhat more difficult to be observed and measured than the radial cracks. As also shown, cracks that extend axially over the CT slice thickness (configuration 1) are detected even if they are about 10 times narrower than the cracks that are narrow in the fuel axial direction (configuration 2). In the interface between two pellets density fluctuations due to pore size distribution are higher than in other cross-sections, the crack detectability is poorer, and cracks wider than in other cross-sections remain undetected.

## DISCUSSION

A radial gradient is observed in all cross-sections measured, Figures 6 and 8. After incorporating corrections for changes in material composition, the observed variations in the density as a function of the pellet radius reflect variations in porosity and pore size distribution, resulting from gas bubble and void formation during irradiation, Figures 6 and 8, right graphs. Except for the mid-sections, the radial gradient is the same for all axial locations measured in fuel Y and for all axial locations in fuel J. The irradiation-induced porosity is the highest in the central region and is lower closer to the pellet periphery: at the fractional radius  $r/R < 0.3$ , it is about 1.5% in fuel Y and 3-4% in fuel J, relative to the pre-irradiation porosity of the corresponding fuel materials, i.e., it is approximately proportional to the fuel burnup. The effect of the presence and distribution of fission products and plutonium on CT density measurements was calculated for known abundance of the corresponding elements and assuming the maximum abundance

fluctuations. It was found to be below  $0.1 \text{ g/cm}^3$  in fuel Y and below  $0.2 \text{ g/cm}^3$  in fuel J, and was included in the CT density measurement error. Because of higher abundance of fission products at the periphery, and the resulting density offset stronger than in the centre, the observed radial density gradients are actually somewhat stronger than those shown in Figures 6 and 8, although within the experimental errors.

The porosity determined in this work from CT density measurements agree with the literature data on the irradiation-induced volume changes in  $\text{UO}_2$  as a function of the fuel temperature [21-24] and with a set of data for swelling measured from volume change using the immersion technique for five CANDU fuel pellets [25, 26]. Up to 4 vol% volume swelling at 2100 to 2300 K has been observed in fuel of 96 to 97% theoretical density, and a maximum of ~9% at 2100 K has been reported [21-24]. Data calculated from volume change using the liquid immersion technique of weighing microsamples for five CANDU fuel pellets irradiated to the burnup of 135 MWh/kg U [25, 26] show an average irradiation-induced porosity of about 0.7 % at  $r/R < 0.7$ , although with a substantial data scatter from -2 to +3 %. A decrease in porosity close to the surface ( $r/R \sim 0.8-1$ ) is explained as the in-reactor densification occurring at temperatures below the out-reactor thermal sintering temperatures. The substantial data scatter that is observed in References [25, 26] at all radii except very close to the pellet surface indicates large experimental errors connected with the liquid immersion method. This method also bears an additional error connected with breaking the fuel into small sections. Because of its porosity, the fuel material has a tendency to break at the locations of large pores and microcracks, which are present in larger volumes in central parts of the fuel than at the periphery and are neglected in density evaluation. In contrast, CT density data are more precise and provide a more representative picture because the measurements are performed on intact fuel sections.

The second feature observed is that the pellet mid-sections ( $x/L \sim 0.5$ ) differ from other cross-sections, i.e., there is an axial density gradient. In both fuels, density is lower in the mid-section than closer to the pellet dish. This is an interesting observation, as no axial density variation was previously observed using ceramography or liquid immersion of microsamples. The pattern of the mid-section radial gradient is different in fuel Y than in fuel J. The axial density variation is not a completely unexpected feature, because of well-documented axial variations in sheath strain due to axial variations in the pellet deformation/swelling and the observation of "secondary ridges" at the mid-section location in fuels irradiated at high-power. The current results indicate that the radial porosity gradient in the pellet mid-section might differ from the radial gradient observed in other axial locations, which should be considered in fuel performance modelling.

Thirdly, we observe that the pellet interface areas in both fuels show material relocation effects, resulting in the expansion of the fuel material into the gap between two pellets. This material expansion has different characteristics in the two fuels. In fuel Y, some material relocation was observed at  $r/R < 0.3$ , and a possible fusion might be occurring in a small part (~3%) of the pellet cross-section. In fuel J, the area where the material expanded into the dish region is bigger, the filling material is more uniform, and the fusion area is bigger, than in fuel Y. The entire central region of  $r/R < 0.4$  is filled up with a highly porous material of a relatively uniform density, and the two pellets are fused over a large area of about 20% of the cross-section. Fusion of two pellets was observed using ceramography in another section of fuel J from the same bundle [27]. It is suggested that the plasticity of the fuel material in the central region  $r/R < 0.4$  caused its expansion into the pellet dish, fusing the two pellets together. Dish filling accompanied by the fusion of two pellets is related to fuel temperature, which is primarily power and fuel burnup dependent. The most probable scenario is that a high power at the beginning of the burnup cycle of fuel J caused fuel plasticity in the central region of  $r/R < 0.4$ , i.e., the region where there was high and a relatively uniform temperature [28], which caused strong material relocation and material bonding over this entire region. This agrees with the observation that the pellet density is uniform in the central region in each cross-section along the element length, including the interface region. Fuel Y was irradiated at a somewhat lower power and to much lower burnup, and the observed material relocation effects are much

less pronounced. The differential thermal expansion and plasticity that contribute to dish filling will, on cooling, also cause the reduced density within the pellet, an effect that might explain the observed higher porosity in the mid-sections of the fuel pellets. Depending on the power and burnup, fission gas bubble formation is a likely contributing factor to both phenomena, especially for fuel J.

The fourth observation is the lack of evidence of circumferential cracks in fuel J. This is in contrast to both the extensive prior evidence from ceramographic observations of circumferential cracking in CANDU fuel and the presence of circumferential cracking in fuel Y. In fuel Y, typical post-irradiation cracking pattern was observed, with both radial and (at least sections of) circumferential cracks. The absence of circumferential cracking in fuel J agrees with ceramographic observations for some other elements of this fuel [27] and might be a characteristic of a high-burnup fuel. The observation of only fragments of circumferential cracks in fuel Y indicates that only crack sections that are sufficiently wide or deep are reproduced while narrower sections are not. No evidence of circumferential cracking in fuel J indicates that they must be tighter than radial cracks in the radial or axial (or both) direction(s), and tighter than circumferential cracks in fuel Y. As shown in Table 1, the width of the narrowest cracks that are observed is  $\sim 5 \mu\text{m}$  for configuration 1 and  $\sim 60 \mu\text{m}$  for configuration 2. Apparently circumferential cracks in fuel J, if present at all, are narrower.

One limitation of the current set-up is that an up to 3 cm long section of the fuel element must be cut for examination in segments with a maximum length of 3 cm. The ability to handle whole fuel elements rather than small sections would require the use of the scanner located in a shielded pit, as described in ref. [7]. Using the current spatial resolution, individual pores are not resolved and the data describe the porosity averaged over at least one pixel volume. Although pores are not resolved and cannot be individually sized, some information on the pore-size distribution can be extracted from the increase in the density standard deviation when compared to the image noise or to the measurements for an unirradiated pellet. This method can be used for both qualitative and quantitative evaluation. In porosity measurements, CT is complementary to SEM: SEM can measure the size and location of individual pores, but not the average volume fraction; CT measures the average volume pore fraction and its distribution, but not individual bubble size nor location within the grain. CT can replace porosity measurement using liquid immersion of microsamples, offering potentially higher accuracy, lower personnel doses, and more information over a larger examination volume with the same technical effort. This is because it is relatively easy to measure several cross-sections in the fuel pellet, once the fuel pellet is positioned on the scanner, and a large number of microsamples can be selected mathematically from the CT image data.

## SUMMARY

Computerised tomography techniques were used in this work to map density or porosity as a function of radial and longitudinal position in a fuel element, and to provide quantitative values of local density as a function of position. The technique is non-destructive and non-invasive, so the examined fuel section is intact and can be subsequently examined by other methods. Radial density gradients are measured by averaging the density data over areas selected mathematically from the measured CT data, which correspond to selecting microsamples without sectioning the fuel. Data are archived and can be subsequently used to perform additional evaluation. CT also provides information on cracking patterns and the relocation of fuel material. Cracks of sizes down to several times smaller than the spatial resolution of the CT image were detected and sized. The CT emission mode was used to map the distribution of radioactive species.

The post-irradiation characteristics observed and discussed in this work for two specimens must be verified by performing measurements on a larger sample of fuel pellets. A more systematic study is also needed to evaluate which of the observed features are caused by the fuel burnup, changing reactor power

characteristics, untypical pre-irradiated fuel properties, and other factors.

This work shows that we currently have a unique quantitative method for non-destructively mapping porosity and cracking in irradiated fuel, and it illustrates basic features of this CT-based technique and the data that can be obtained. Techniques developed in this work can be used to characterise CANDU reactor fuel before and after irradiation.

## ACKNOWLEDGEMENTS

Discussions of various aspects of this work with R.A. Verrall, W.H. Hocking, M.R. Floyd, J.D. Sullivan, M. Tayal, J.A. Sawicka, Z. He, F.C. Dimayuga, and others are appreciated. Technical assistance provided by P.W. Reynolds, R. Roiha and R. Stothers is acknowledged.

## REFERENCES

1. B.D. Sawicka and B.J.F. Palmer, "Application of Computed Tomography to the Development of Advanced Ceramics", presented at the International Symposium on Fine Ceramics Arita 1988, Arita, Japan, 1988 November, in Arita Conference Proceedings (1989), also Journal of Canadian Society for Nondestructive Testing **10**, No. 2 (1989) 24-33.
2. B.D. Sawicka and B.J.F. Palmer, "Density Gradients in Ceramic Pellets Measured by Computed Tomography", Nuclear Instruments and Methods in Physics Research **A263** (1988) 525-528.
3. J. Sullivan, J. Root, B.D. Sawicka and J. Glass, "Non-Destructive Evaluation of Infiltration Toughened Ceramics", AECL Report, AECL-9728 (1988), also B.D. Sawicka, J. Sullivan, J. Root and J. Glass, "Computed Tomography and Neutron Scattering Study of Zirconia Toughened by Alumina", Ceramics Eng. Sci. Proc. (American Ceramic Society) **9-10** (1988) 1491-1502.
4. B.D. Sawicka, J.G. Murphy, F. Taheri and L.E. Canary, " $\gamma$ -ray CT Examination of Density Gradients in Slip Cast Ceramics: Correlation with Stress Distribution", Nuclear Instruments and Methods in Physics Research **B69** (1992) 365-369.
5. P. Sutton, L.R. Hillier and B.D. Sawicka, "Computed Tomography and Ultrasonic Testing of Urania Pellets", in *Review of Progress in Quantitative Nondestructive Evaluation* (D.O. Thompson and D.E. Chimenti, editors), Vol. 8B, Plenum Press, New York and London (1989) 1693-1700, ISBN-0-306-43209-9.
6. B.D. Sawicka, "CT Sensitivity for Detecting Defects", AECL Report, RC-1168 (1993).
7. B.D. Sawicka, R.V. Murphy, G. Tosello, P.W. Reynolds and T. Romaniszyn, "Computed Tomography of Radioactive Objects and Materials", Nuclear Instruments and Methods in Physics Research **A299** (1990) 468-479.
8. B.D. Sawicka and R.A. Verrall, "CT Measurements of Irradiated Fuel", presented at the 30th International Nuclear Fuel Performance Conference, Seattle, WA, 2000 July 23-26.
9. G.T. Hermann, *Image Reconstruction from Projections: The Fundamentals of Computerized Tomography*, Academic Press, New York, NY (1980).
10. W.M.J. Veigele, "Photon Cross-Sections from 0.1 keV to 1 MeV for Elements Z=1 to Z=94", Atomic Data Tables **5** (1973) 51-111.
11. J.H. Hubbell, "Photon Mass Absorption and Energy-Absorption Coefficients from 1 keV to 20 MeV", Int. J. Appl. Radiat. Isot. **33** (1982) 1269-1290.
12. G.X. Ritter and J.N. Wilson, *Handbook of Computer Vision Algorithms in Image Algebra*, CRC Press, Inc., Boca Raton, FL (1996).
13. J.C. Russ, *The Image Processing Handbook*, CRC Press, Inc., Boca Raton, FL (1999) ISBN 0-8493-2532-3.
14. P.D. Tonner and G. Tosello, "Experience with a Versatile CT Test Bed", in *Industrial Computerized Tomography*, The American Society for Nondestructive Testing, Inc., Seattle, WA (1989) 18-23, ISBN 0-931403-89-8.

15. P.D. Tonner, B.D. Sawicka, G. Tosello and T. Romaniszyn, "Region-of-Interest Tomography Imaging for Product and Material Characterization", in *Industrial Computerized Tomography*, The American Society for Nondestructive Testing, Inc., Seattle, WA (1989) 160-165, ISBN 0-931403-89-8.
16. B.R.T. Frost (editor), "Nuclear Materials", Volumes 10A and B, in *Materials Science and Technology* (BR.W. Cahn, P. Haasen and E.J. Kramer, editors), VCH Publisher Inc., New York, NY (1994).
17. H.J. Smith, J.C. Tait and R.E. Von Massow, "Radioactive Decay Properties of Bruce A CANDU UO<sub>2</sub> Fuel and Fuel Recycle Waste", AECL Report, AECL-9072 (1987).
18. R. Jones, AECL, personal communication.
19. R.S. Dickson, AECL, personal communication.
20. B.D. Sawicka and R.L. Tapping, "CAT Scanning of Hydrogen Induced Cracks in Steel", *Nuclear Instruments and Methods in Physics Research A* **256** (1987) 103-111.
21. D.O. Pickman, D.H. Willey, and V.M. Eldred, "SGHWR Fuel Elements Performance", in *Nuclear Fuel Performance: Proc. Int. Conf. of British Nuclear Energy Society*, British Nuclear Energy Society, London (1973) 51.1- 51.6.
22. D.A. Collins and R. Hargreaves, ref. [21], 50.1-50.5.
23. K.S. Rose, J. Williams and G. Potts, "Technique for Measuring the Density of Small Fragments of High Density Materials Both Before and After Irradiation", *Journal of Nuclear Materials* **51** (1974) 195-198.
24. A. Hoch and H. Matzke, "Fission-Enhanced Self-Diffusion of Uranium in UO<sub>2</sub> and UC", *Journal of Nuclear Materials* **48** (1973) 157-164.
25. I.J. Hastings, M.J.F. Notley and D.H. Rose, "Irradiation-Induced Volume Changes in UO<sub>2</sub>", *Journal of Nuclear Materials* **75** (1978) 301-303.
26. I.J. Hastings, D.H. Rose and M.H. Schankula, "Volume Changes in Irradiated UO<sub>2</sub> Fuel", *Journal of American Ceramic Society* **58** (1975) 74.
27. M.R. Floyd, AECL, personal communication.
28. H. Bailly, D. Menessier, C. Prunier (editors), *The Nuclear Fuel of Pressurized Water Reactors and Fast Reactors: Design and Behaviour*, Lavoisier Publishing Inc., Paris, France; Intercept Ltd, Hampshire, UK; c/o Springer Verlag, NJ, USA (1999).

Table 1: The width of the smallest crack (in  $\mu\text{m}$ ) that can be measured from an 80- $\mu\text{m}$ -pixel CT scan

Crack length Contrast (%)	Configuration 1			Configuration 2		
	5 pixels (0.4 mm)	10 pixels (0.8 mm)	80 pixels (6 mm)	5 pixels (0.4 mm)	10 pixels (0.8 mm)	80 pixels (6 mm)
1	1 - 2	<1	0.3	26 - 33	22 - 28	13 - 16
2	1.5 - 2	1- 1.5	0.5	40 - 46	32 - 40	19 - 23
5	<b>3.5 - 5</b>	<b>2.5 - 4</b>	1 - 1.3	<b>60 - 73</b>	<b>50 -60</b>	30 - 37
10	7 - 11	5 - 8	2 - 3	85 - 105	70 - 90	45 - 55

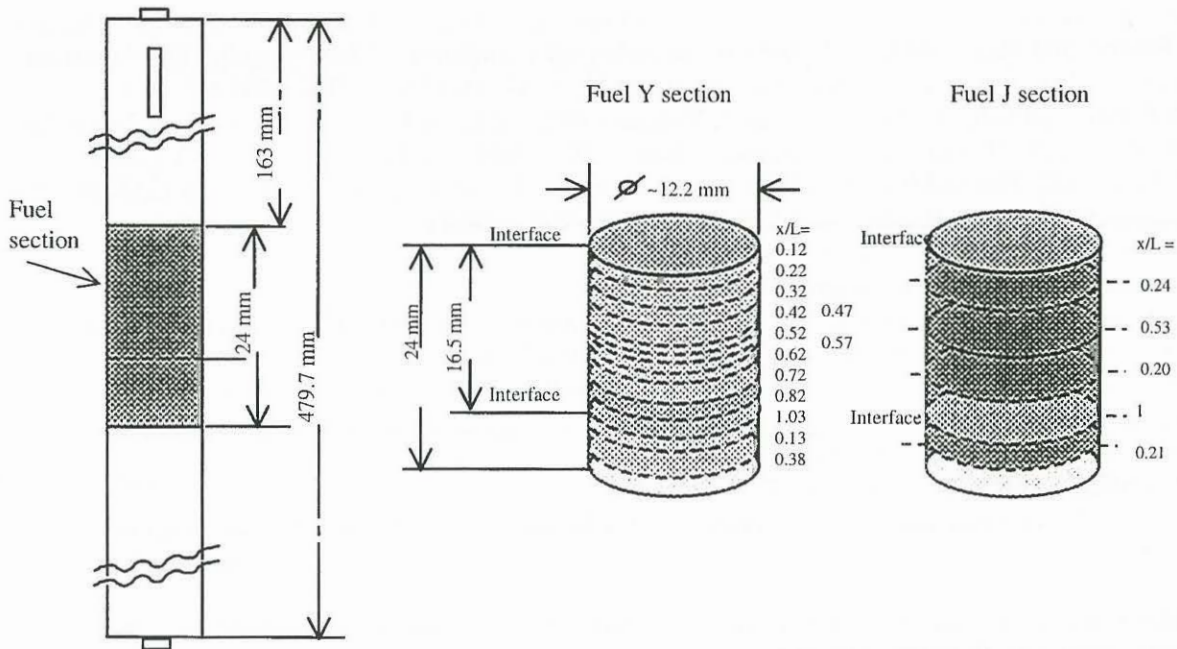


Figure 1: Left: Geometry of the fuel section cut from two fuel elements for CT examination. Right: Location of CT-measured cross-sections for the examined sections in fuels Y and J.

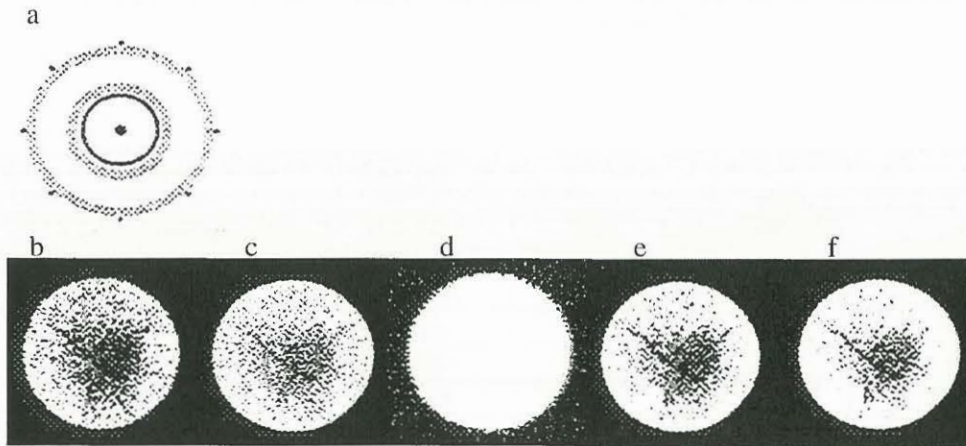


Figure 2: Six CT images measured for the mid-section of fuel pellet J. Image (a) shows a standard CT scan of the pellet and flask area: the fuel pellet is a black dot in the centre represented by 17 pixels.

Images (b) to (f) show ROI scans of the pellet area: (b) the pellet cross-section is reconstructed using about 4000 pixels; (c) the pellet cross-section is reconstructed using about 20,000 pixels; (d) is the same as (c) but using a low-range density scale to show the Zircaloy sheath rather than the fuel material; (e) and (f) were obtained from image (c) after mathematical processing, that resulted in better image contrast and some degradation in the spatial resolution.

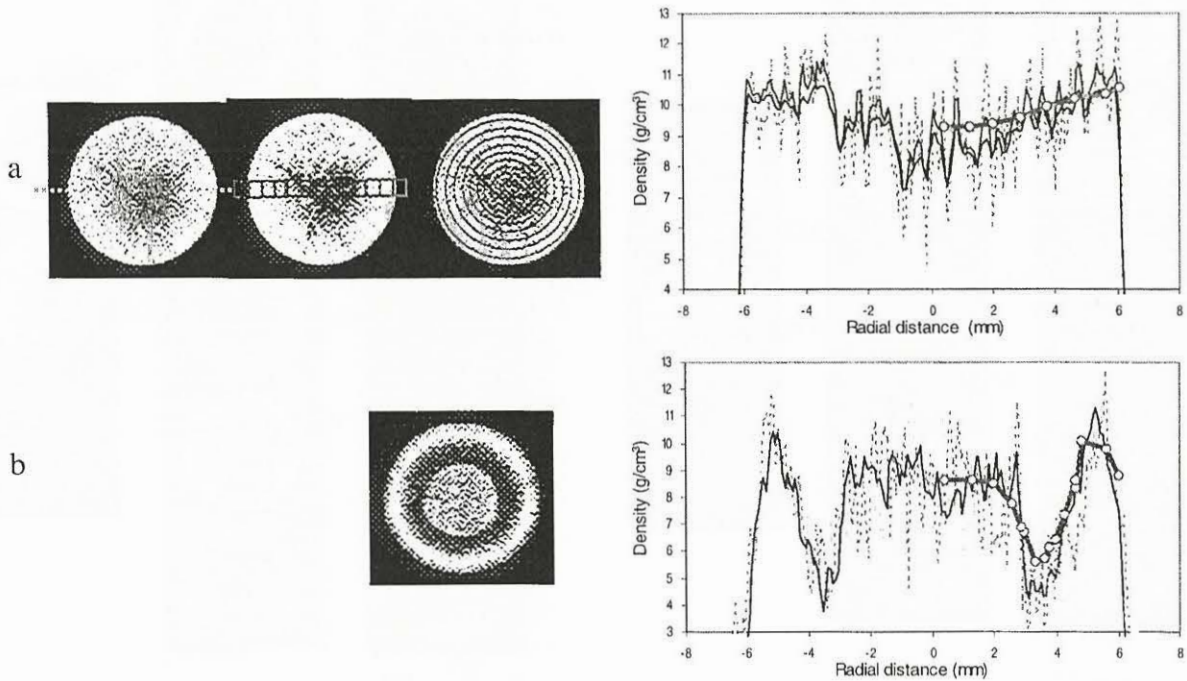


Figure 3: Evaluation of radial density gradients from the CT image data. Graphs show the density variation along the pellet diameter for two cross-sections in the fuel J pellet: the mid-section (a) and the dish region (b). Three methods of radial density evaluation are illustrated by patterns superimposed on image (a): dotted lines show density profiles at the pixel level; thin solid lines are for CT data integrated over four-pixel “microsamples” along the pellet diameter; and thick solid lines represent averaging over many pixels at selected radii marked by circles.

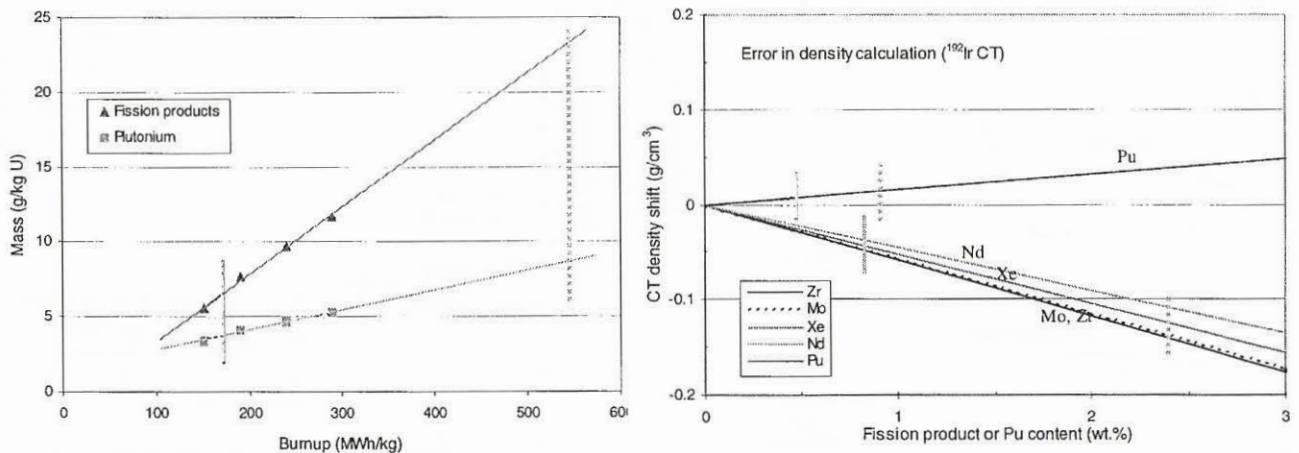


Figure 4: Left: Inventory of major fission products and plutonium in used fuel calculated for Bruce CANDU  $\text{UO}_2$  fuel as a function of burnup, after more than one year out-of-reactor, from [17]. Right: Density offset caused by the neglected presence of fission products and Pu, calculated as a function of their abundance in irradiated  $\text{UO}_2$ . Vertical lines mark estimates for fuel Y (solid line) and fuel J (dotted line).

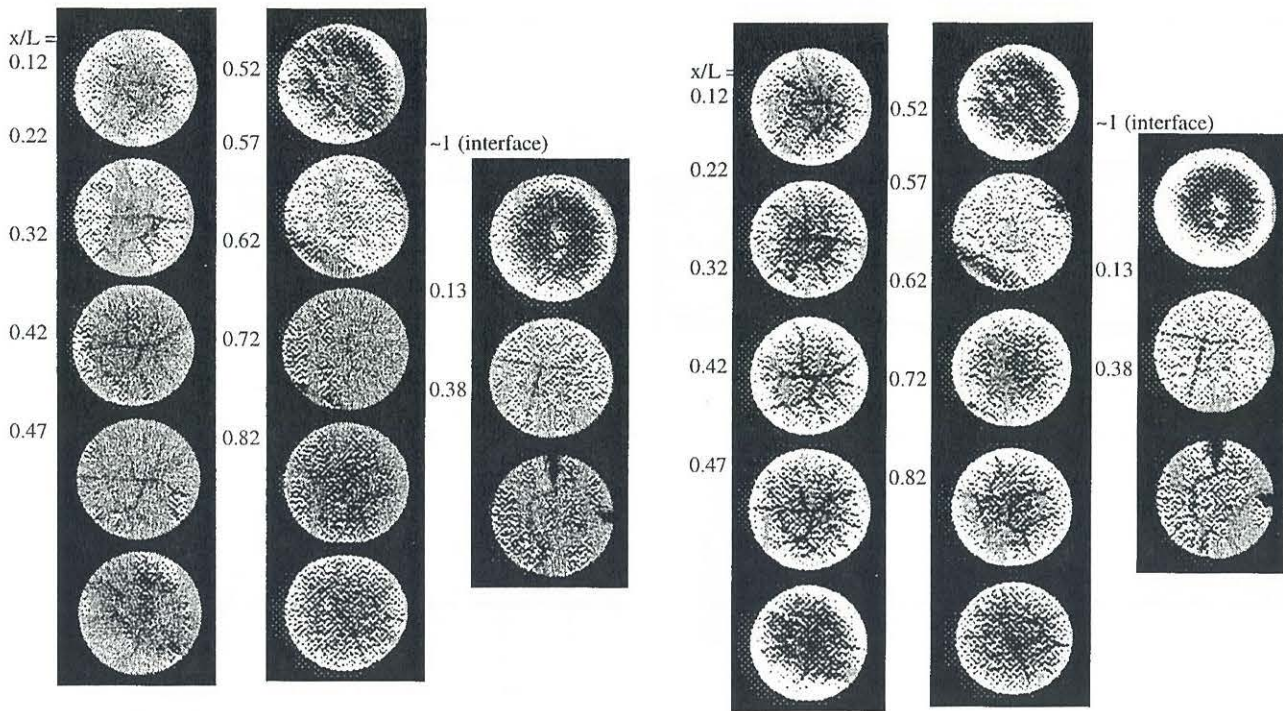


Figure 5: Thirteen radial cross-sections measured for the fuel Y. Left: The pixel size is 80  $\mu\text{m}$ , the spatial resolution is 160  $\mu\text{m}$  and the image contrast is 4% to 10%. Right: The same images after 5-point Gaussian filtering.

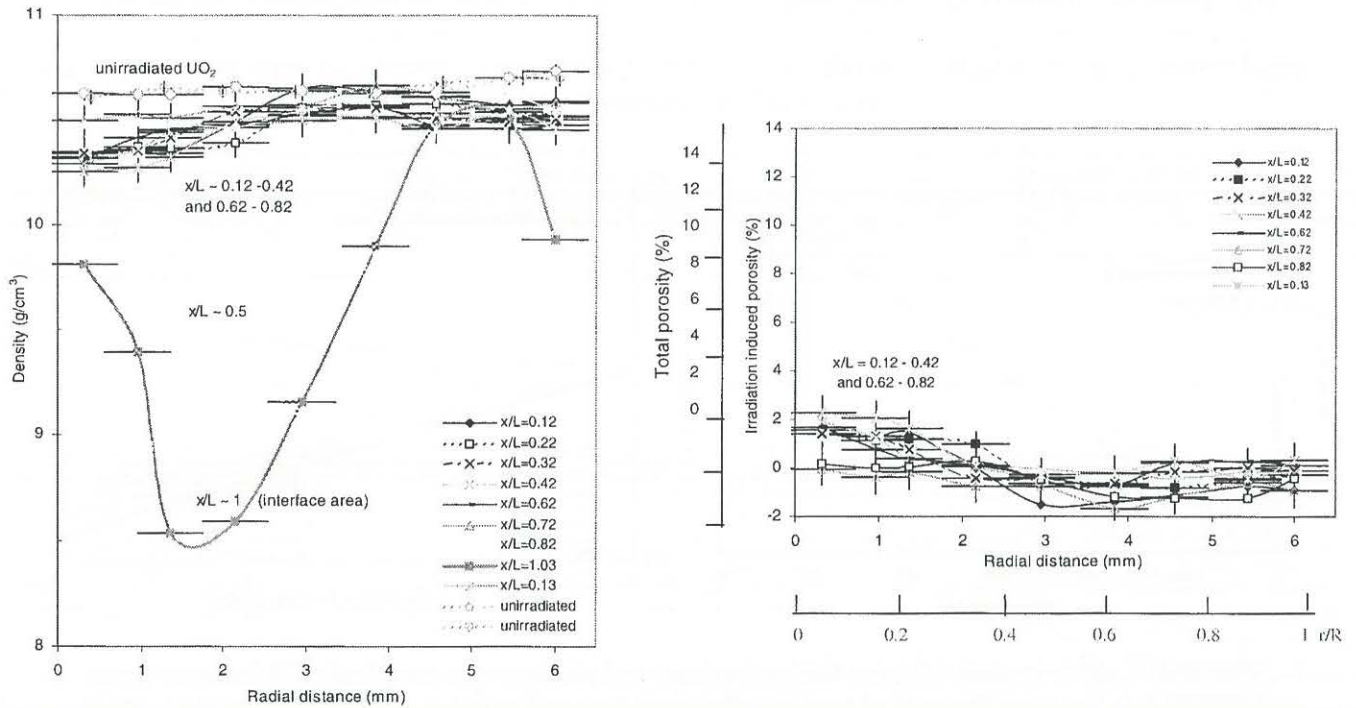


Figure 6: Left: Density as a function of pellet radius for the section of fuel J, calculated by averaging the CT data over concentric rings and the central circle. Right: Radial variation of the irradiation-induced porosity.

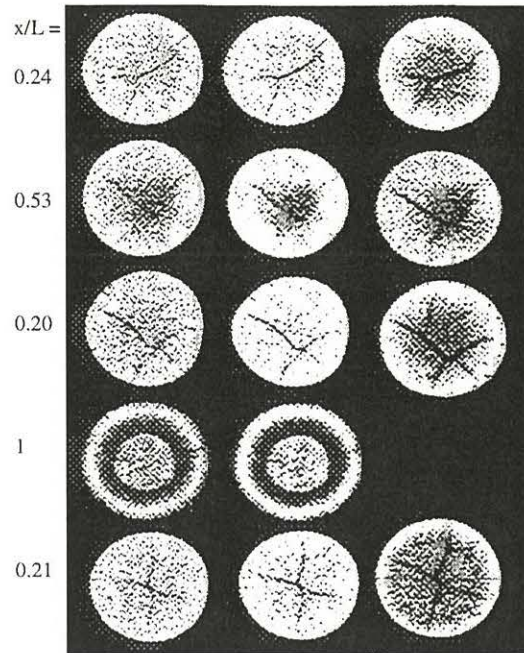


Figure 7: Five radial cross-sections measured for the fuel J. Left column: CT images measured using a pixel size of  $80\ \mu\text{m}$  and an image contrast of about 10%. Middle column: The same images after four-pixel averaging. Right column: CT images measured using a pixel size of  $160\ \mu\text{m}$  and an image contrast of 1-3%.

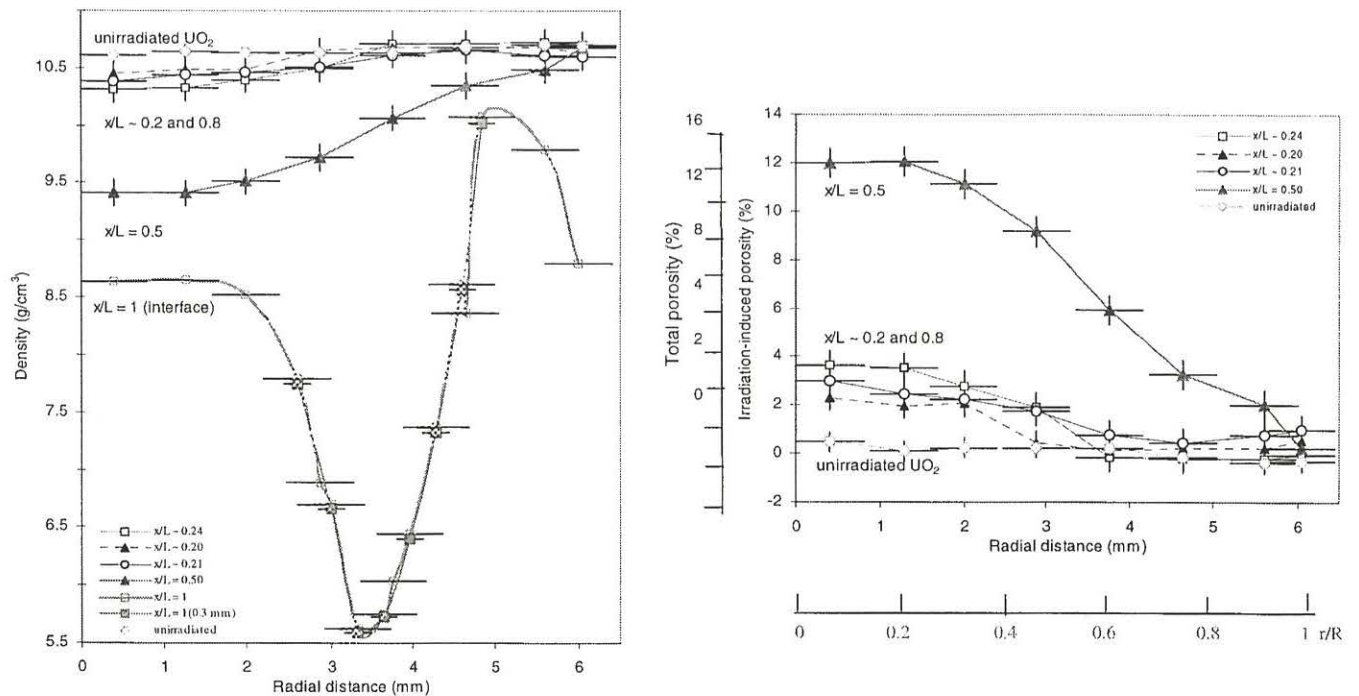


Figure 8: Left: Density as a function of pellet radius for the section of fuel J, calculated by averaging the CT data over concentric rings and the central circle. Right: Radial variation of the irradiation-induced porosity.